Tellus (2005), 57A, 136–152
Printed in UK. All rights reserved

TELLUS

Southwesterly flows over southern Norway—mesoscale sensitivity to large-scale wind direction and speed

By IDAR BARSTAD[1] and SIGBJØRN GRØNÅS[2]*, [1]*Institute for Energy Technology, 2027 Kjeller, Norway;* [2]*Geophysical Department, University of Bergen, 5007 Bergen, Norway*

(Manuscript received 17 October 2003; in final form 1 November 2004)

ABSTRACT

Mesoscale structures have been identified and studied for simulations of ideal flows passing southern Norway. The large-scale wind direction was between south and west and the wind speed between 10 and 22.5 m s^{-1}. Flow data have been provided from simulations with a mesoscale numerical model with 10 km between the grid points horizontally. The results are found to be qualitatively in accordance with observational findings, including old forecasting rules for southern Norway. As expected, the influence of rotation is considerable. Accordingly, the flows are characterized by a jet on the left side of the mountains and a minimum on the right upstream side. In addition, a wind shadow extends far downstream of the main mountains, with signs of increased winds on the right side of the wind shadow. The wind shadow is connected to an inertio-gravity wave with downstream signatures caused by rotation. When the background wind direction was turned, the alignment of the structures was turned accordingly. For flows in the sector 200–270°, the action of the Coriolis force gave an efficiently narrower mountain (than without rotation). A similar action for southerly flows, on the other hand, resulted in an efficiently wider mountain. Different mountain widths resulted in different shape of the gravity waves and different acceleration of the jet on the left side. When the wind speed is increased, the amplitudes of the mesoscale structures are decreased with no abrupt change in the character of the flow.

1. Introduction

To a large extent, variation in local weather and climate in Norway is caused by effects of the mountains on the large-scale air currents. The Bergen School meteorologists studied flows over southern Norway from surface observations in a rather dense network (Bjerknes and Solberg, 1921, 1922). As the data record increased, the forecasters in Bergen made rules for wind and precipitation forecasting in flows with different air masses from different directions. In due time their findings were carefully documented by Spinnangr (1942, 1943a,b). In addition to the distribution of orographic precipitation, the forecast rules included strong coastal winds on the left side of the mountains (called corner jets by Bergeron, in Godske et al., 1957, p. 607), and wind shadows on the lee side. Even today, the results are being used with success in daily weather forecasting. Since the days of the pioneers, just a few papers related to flows over Norway have been published. Andersen (1973, 1975) describes the distribution of surface winds and precipitation over southern Norway in some weather classes defined by the geostrophic wind. Nordø and Hjortnæs (1966) give statistical relationships between precipitation and parameters like the onshore geostrophic wind component. A survey of literature, including reports published outside meteorological journals, was given by Smith (1979). Since 1979 no peer reviewed paper on flow over southern Norway has appeared.

In this paper idealized flows over realistic mountains representing southern Norway are studied for large-scale flow directions in the sector from south to west. The main purpose is to identify the main mesoscale structures set up by the mountains and to investigate how they vary with large-scale wind direction and wind speed. We will also seek updated physical explanations for the main variations identified. Along these lines we seek increased basic knowledge for weather prediction in the area.

The topography of southern Norway includes a plateau (Hardangervidda), steeper ranges on smaller scales, valleys and narrow, long fjords (Fig. 1). A typical horizontal scale L (half-width) of the main range varies from 100 km for westerly wind to 250 km for southerly winds. A typical height h is 1500 m (isolated tops reach more than 2400 m). For upstream wind speed U in the range from 5 to 20 m s^{-1}, the Rossby number of the perturbations set up by the mountains—$Ro = U/Lf$, where f is the Coriolis parameter—varies between 0.15 and 0.65 for southerly winds and from 0.40 to 1.65 for westerly winds. Accordingly, the effect of rotation plays a significant, but not

*Corresponding author.
e-mail: sigbjorn@gfi.uib.no

Fig 1. Inner integration area and topography of southern Norway (contours every 200 m). The main regions are Østlandet, Sørlandet, Vestlandet, Møre, Trøndelag and Nordland. The border with Sweden is marked. Positions along the coast are related to the names of the main fjords (indicated by arrows from the names). In addition, the corner points of Stadt, Lista and Lindesnes are marked. The mountain plateau Hardandervidda is indicated, and the highest mountain areas mentioned in the text are: Jotunheimen (peaks to 2400 m) and Sylane (1800 m).

dominant, role in the perturbations. For this range in winds, the flows will be in the intermediate flow domain ($Ro \sim 1$; e.g. Trüb and Davies, 1995), between quasi-geostrophic flows, characterized by a shallow anticyclone over the mountain (Smith 1979, 1980), and mountain flows without rotational effects (e.g. Smith, 1989a; Smolarkiewicz and Rotunno, 1989, 1990; Smith and Grønås, 1993; Baines, 1995; Ólafsson and Bougault, 1996, 1997). Theoretical investigations on flows in the intermediate domain ($Ro \sim 1$) have been carried out by, for example, Smith (1982), Pierrehumbert and Wyman (1985), Trüb and Davies (1995), Thorsteinsson (1988), Thorsteinsson and Sigurdsson (1996), Ólafsson and Bougault (1996), Hunt et al. (2001) and Petersen et al. (2003).

Simple flows without rotation and friction are controlled by the non-dimensional mountain height $\hat{h}$, defined as $\hat{h} = Nh/U$, where N is the Brunt–Väisälä frequency. Three flow regimes are expected: one characterized by gravity waves ($\hat{h} < 1$); one with upstream stagnation, flow splitting around the mountains and a downstream wake ($\hat{h} \gg 1$); and one with a high drag over the mountains, strong lee winds and breaking gravity waves aloft ($\hat{h} \sim 1$) (Smith 1989a). For $h \sim 1000$ m and normal values of U and N, all three regimes should be present at smaller-scale mountains in southern Norway.

For several reasons flows over southern Norway are more complex than in the mentioned theory. The mountain shapes are irregular with steep slopes and several surface types are present, first of all sea and land. The complex conditions have led us to include friction and diabatic effects in the main simulations. However, the upstream humidity profile has been kept rather dry. In this way release of latent heat has had little influence on the results. We have limited the study to effects of the largest scales of the mountains of southern Norway. Accordingly, the numerical model, described in Section 2, has been run with a grid size of 10 km (39 vertical levels). Winter conditions have been selected for radiation and sea surface temperature.

The main set of experiments was run for large-scale wind directions every 10°, with a fixed large-scale wind speed and a fixed Brunt–Väisälä frequency. For one large-scale wind direction, experiments with different wind speeds have been made. In Section 3 some mesoscale structures are identified, and it is described how they vary with wind direction and wind speed. In Section 4 we quantitatively compare the results found in Section 3 with the forecasting rules of Spinnangr (1942), observed wind distributions presented by Andersen (1975) and our own observational evidence. A discussion on the dynamical causes for the mesoscale variations is found in Section 5 and concluding remarks in Section 6.

2. The numerical model and the set-up of experiments

Experiments have been made with the fifth-generation PSU/NCAR (MM5) numerical mesoscale model. A detailed description of the model is given by Grell et al. (1994). The model, which runs on polar stereographic coordinates, has two grids: an outer grid with 30 km horizontal grid length and an inner with 10 km grid length. The two grids have been horizontally nested, in such a way that information is exchanged mutually (two-way nesting). The outer grid has the dimension of 60 × 66 grid points, and the inner 100 × 94 (see Fig. 1 for the inner domain). The boundaries of the outer grid are placed 90 km upstream of the inner grid's boundaries. The topography is derived from US Geological Survey database. In the vertical, a sigma coordinate was used, allowing the model surfaces to follow the terrain near the ground. A total of 39 layers have been used, with 17 layers in the lower 1200 m. The top layer is placed at 10 hPa.

The radiation scheme interacts with the atmosphere, clouds, precipitation fields and the surface (Dudhia, 1989). The explicit moisture scheme has prognostic equations for water vapour, cloud liquid water (or ice below 0 °C) and rain water (or snow), and allows supercooled water to exist below 0 °C. Convection was parametrized according to Dudhia (1989). A second-order closure scheme based on Burk and Thompson, (1989) is used for the parametrization of heat and momentum fluxes in the boundary layer. The surface scheme is based on a "force-restore" method (Blackadar, 1979; Zhang and Anthens, 1982).

The starting fields have been in geostrophic and hydrostatic balance on an f plane ($f = 1.24 \times 10^{-4}$ s^{-1}). In all experiments the wind direction, wind speed as well as humidity and temperature were kept constant at the lateral boundaries of the coarse grid. The sea surface temperature was set to 281 K, and the temperature variation with height was constructed by integration of the hydrostatic equation expressed by the Brunt–Väisälä frequency N, that was kept constant equal to 0.012 s^{-1} up to 300 hPa. Towards 150 hPa, the static stability has been steadily increased to $N = 0.017$ s^{-1}. A constant profile of relative humidity was used: 0.6 below 700 hPa, 0.5 between 700 and 500 hPa, 0.3 between 500 and 300 hPa and 0.05 above. The simulations were run with radiation conditions for mid-winter; however, no snow cover was present.

In the presence of realistic mountains, the starting procedure may influence the results for some time after start-up. To avoid the initially "warm mountain" influencing our results, two starting procedures were tested. In the first we slowly increased the wind speed from zero to full wind speed, and in the second we used an impulsive start with full wind speed from the beginning. Both methods show similar results after 24 h integrations; a result in accordance with Smolarkiewicz and Rotunno (1989). We have chosen the latter start-up procedure. The simulations were run to at least $tU/L = 12$ normalized time units, where t is the integration time in seconds. The amplitudes of the buoyancy waves towards the upper boundary are nicely dampened, and no sign of reflection from the upper boundary has been seen.

3. Mesoscale structures

The large-scale wind direction is denoted by the upstream surface isobars at 5°E. Two sets of simulations were made: (a) for large-scale wind direction every 10° between 170 and 260° with a large-scale wind speed of 15 m s^{-1} above the boundary layer; (b) for two additional wind speeds, 10 and 22.5 m s^{-1}, for a wind direction of 230°. Results from (a) are presented in Section 3.1 and results from (b) in Section 3.2.

3.1. Variation with wind direction

The flows from the three directions 230, 170 and 200° are shown in Figs. 3, 4 and 5 respectively. Each figure shows horizontal wind maps for three levels and three cross-sections (potential temperature and wind speed). The three levels are: 100 m above the ground, referred to as the surface; approximately 700 m above the ground, close to the strongest winds set up by the mountains; and at approximately 1800 m, where clear signs of inertio-gravity waves are illustrated through vertical velocity. Strong friction over land decreases the wind close to the ground. The lowest level at 100 m is chosen to more clearly estimate the wind at exposed places over mountainous terrain. The positions of the three cross-sections are shown in Fig. 2. Section I is a fixed section across the coast south of Stadt. Sections II and III are across

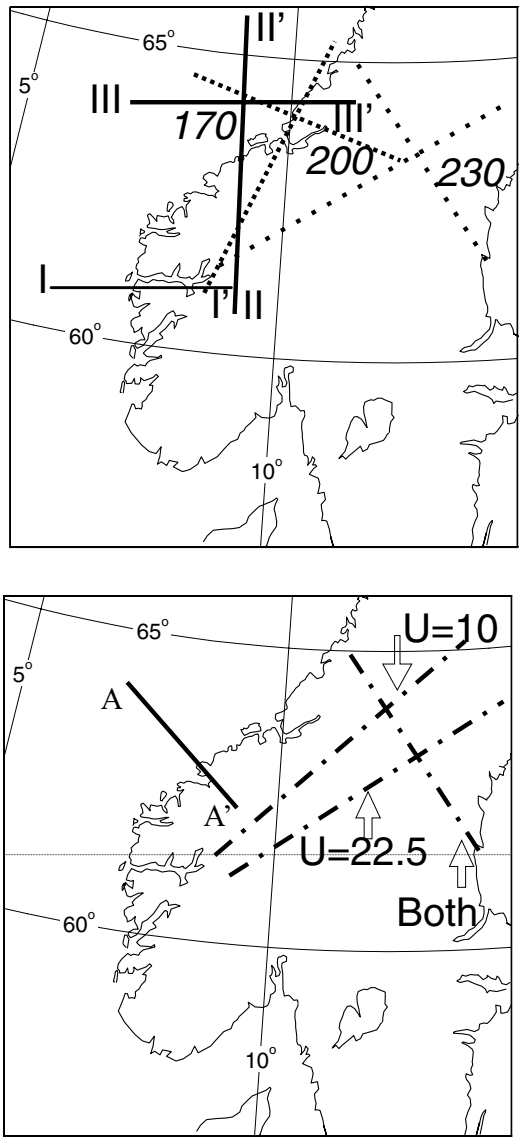

Fig 2. Positions of three cross-sections I, II, III presented in the subsequent figures. Upper panel: Sections used in Figs. 3, 4 and 5 for large-scale wind speed 15 m s^{-1} and directions 230, 170 and 200°. Section I (marked I–I′) is fixed for the three directions. Sections II and III (marked II–II′ and III–III′) are along and across the downstream wind shadow and vary with direction. Lower panel: Cross-sections II and III used Figs. 6 and 7 for large-scale direction 230° with wind speeds 10 and 22.5 m s^{-1} respectively. Cross-section AA' is used in Fig. 11.

and along the main flow downstream from the highest mountains. The directions vary according to the background wind direction.

As expected from theory cited in the introduction, rotation has a significant influence on the perturbations set up by the mountains. Accordingly, all the experiments show increased wind speed on the left side of the mountain and a wind minimum

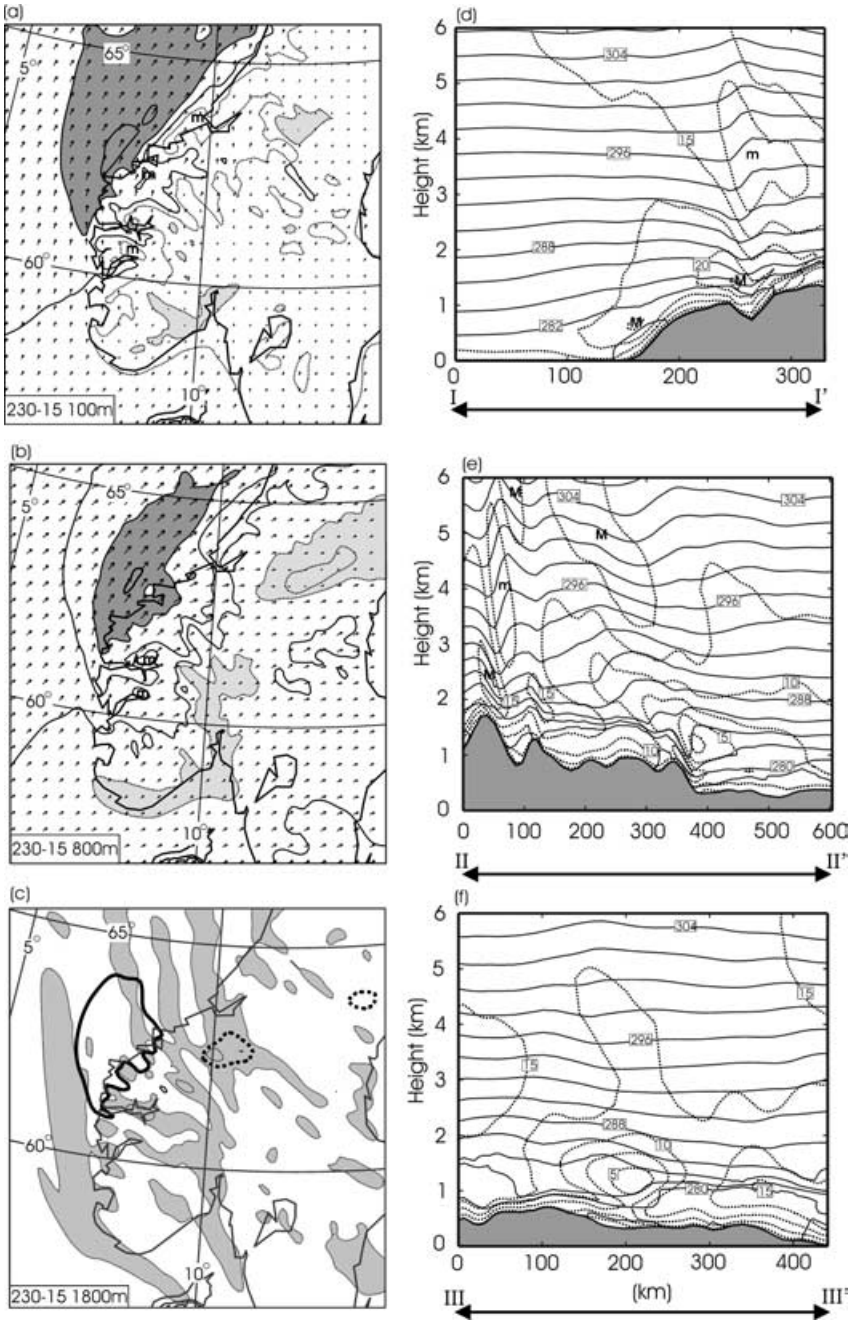

Fig 3. Horizontal wind maps for three levels (left column, isotachs every 4 m s^{-1}) and cross-sections, shown in Fig. 2a, I, II and III (right column) of potential temperature (contours every 2 K) and wind speed (isotachs every 2.5 m s^{-1}) for large-scale wind direction 230° and speed 15 m s^{-1}. Upper left panel: surface (approximately 100 m above ground). Isotachs: solid contours, 12 m s^{-1} and more; stippled contours, less than 12 m s^{-1}. Maximum areas more than 16 m s^{-1} and minimum areas less than 4 m s^{-1} are shaded grey. Other minima are marked with an "m". Middle left panel: aloft (approximately 700 m above ground). Isotachs as before, but solid contours are 14 m s^{-1} and more and stippled contours less than 14 m s^{-1}. Maximum areas more than 22 m s^{-1} and minimum areas less than 10 m s^{-1} are shaded grey (maximum area darker than minimum area). Lower left panel: approximately 1800 m above ground. Isotachs as above, but the contour for 14 m s^{-1} is omitted: heavy solid contours, 18 m s^{-1} or more; heavy stippled contours, wind speed of 10 m $s^{-1}$and less; shaded areas, two stippled contours of negative omega (positive vertical wind component), −0.001 hPa s^{-1} and −0.01 hPa s^{-1}.

on the upstream right side. The increased wind on the left side forms a jet along the mountain slopes and out over the sea, with maximum wind speed approximately at the top of the boundary layer (Figs. 3, 4 and 5, two lowest levels, Section I). This jet will be referred to as *the left-side jet* and the upstream minimum on the right side as *the upstream minimum*. The lowest wind speeds are found in a wind shadow on the lee side, downstream of the highest mountains (Figs. 3, 4 and 5, two lowest levels and Sections II and III). We call this structure *the downstream wind shadow*. North of Stadt, south of Trondheimsfjord, a shallower wind shadow was found for large-scale directions around the southwest (Figs. 3 and 5, surface), here called *the coastal wind shadow*. We also find a secondary area of increased winds to the right of the downstream wind shadow (see Section III, Fig. 3, maximum wind speed at 1 km height). The name *right-side jet* will be used. The flow is otherwise characterized by streamlines crossing the mountains and gravity and inertio-gravity waves with increased wind speeds in the lee of the mountains. Maximum and minimum wind speeds related to the structures briefly described above are given in Table 1 for all main experiments.

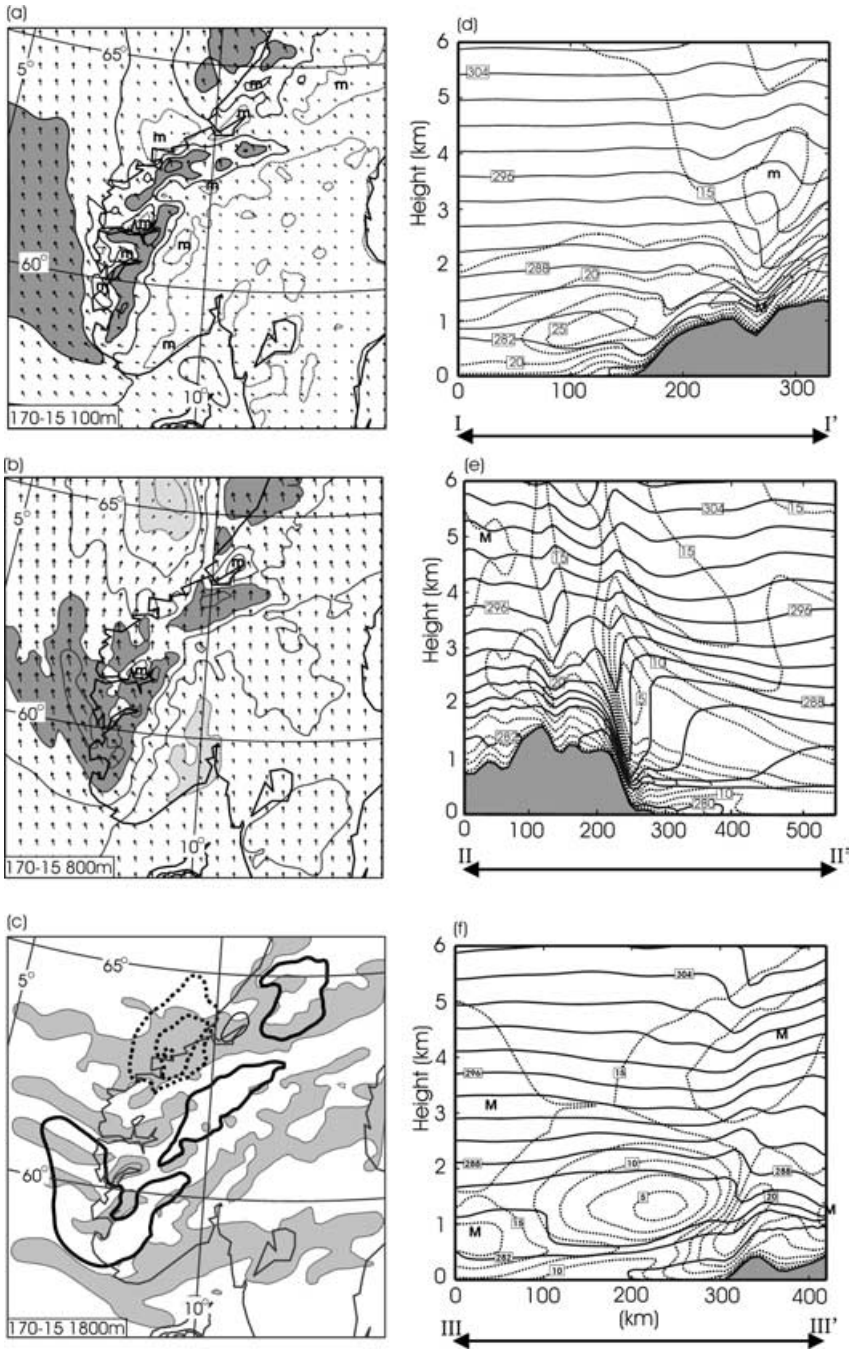

Fig 4. Same as Fig. 3, but for large-scale direction 170°.

The range in wind speed in Table 1 demonstrates that the influence of the mountains is considerable. In the experiments with a large-scale wind speed of 15 m s^{-1}, the strongest wind, found in the left-side jet, is 28.7 m s^{-1} and the weakest wind 1.0 m s^{-1}, found above the boundary layer in the downstream wind shadow.

3.1.1. Large-scale wind direction 230°. The left-side jet is accelerating along the coast of Vestlandet and reaches its maximum over the sea a little downstream of the corner at Stadt. Close to surface (lowest two levels in Fig. 3) the jet extends for several hundred kilometres over the sea northeastwards from Stadt. The axis of the jet curves around the corner at Stadt and forms a small angle with the main coastline north of Stadt. The length scale along the jet is at least the scale of the large-scale mountains of southern Norway in the same direction as the jet. The jet is broadening downstream along the coast of Vestlandet, south of Stadt. The scale across the jet seems to reach the same scale as the mountains in the same direction. The maximum

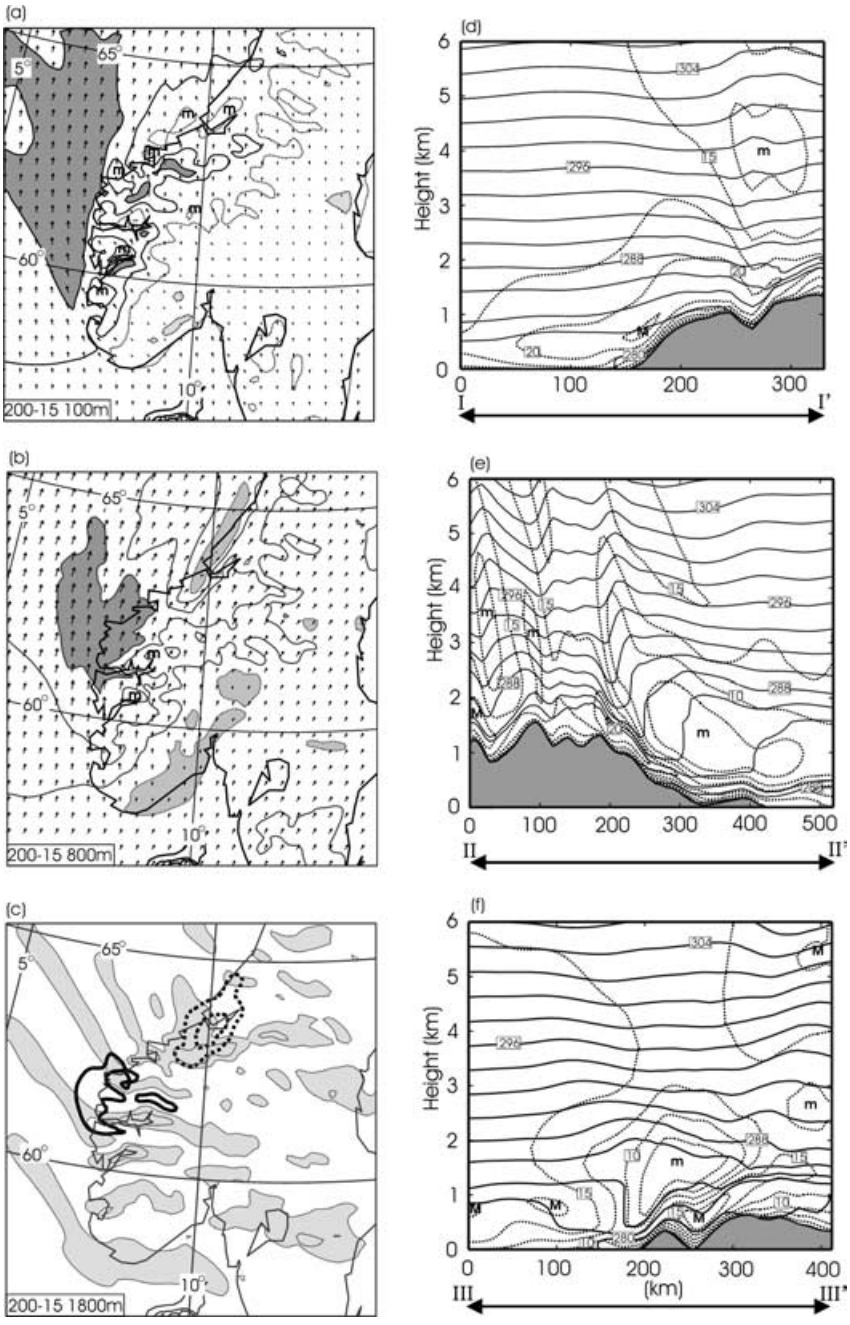

Fig 5. Same as Fig. 3, but for large-scale direction 200°.

wind speed is 26.8 m s^{-1} close to the middle level in Fig. 3. Compared with other large-scale directions, the jet is now at its strongest at the surface (maximum 21.1 m s^{-1} at the lowest level). The strongest winds are here found over the sea, where surface friction is far less than over land. Along the coast, coastal convergence seems to contribute to increased wind just off the coast. At the upper level the area of strong wind on the left side of the mountains loses its elongated structure, i.e. the scale along the jet becomes of the same order of magnitude as the scale across it. The area of increased wind on the left side is noticed to high levels, but above 2500 m over the topography the perturbations are small.

At the surface the upstream minimum is seen inside the coast at Lindesnes, and a little west of Lindesnes aloft (horizontal maps in Fig. 3). The vertical extent is about 2000 m, a little less than for the jet. There is no sign of upstream stagnation, at the middle level the minimum wind speed is 7.8 m s^{-1}. In the lowest two levels in Fig. 3 the minimum area extends eastwards along the

Table 1. Maximum (minimum) wind speed (m s^{-1}) in the different experiments for the left-side jet, the upstream minimum, the downstream wind shadow, the wind increase on the right side of the wind shadow (right-side jet) and the maximum lee wind. The latter is found south of Stadt (Sognefjord and Hardangerfjord) for directions 170, 180 and 190°, just north of Stadt for 200, 210, 220 and 230° and north of Romsdalsfjord for 240, 250 and 260°

Large-scale direction (deg) and speed (m s^{-1})	Jet aloft (around 700 m)	Jet surface (at ∼100 m)	Upstream minimum (at ∼700 m)	Downstream min. aloft	Right side jet aloft	Lee wind aloft	Lee wind surface (at ∼100 m)
170, 15	28.7	19.3	7.6	2.8	24.5	29.1	24.0
180, 15	26.4	19.4	7.9	1.3	22.4	26.7	21.5
190, 15	26.1	19.5	7.7	1.7	24.0	25.0	19.5
200, 15	25.6	19.6	7.2	4.8	22.0	26.5	18.2
210, 15	25.0	20.2	7.3	4.0	19.0	26.0	17.0
220, 15	25.8	21.1	7.5	1.7	16.5	25.3	16.1
230, 15	26.8	21.0	7.8	1.0	17.1	25.3	16.2
240, 15	26.9	20.7	7.7	2.0	15.1	25.3	17.1
250, 15	26.2	20.7	8.4	3.5	14.2	25.2	17.5
260, 15	25.4	20.4	7.9	3.9	15.2	24.5	21.5
230, 10	21.5	18.3	1.4	0.9	11.6	17.5	12.6
230, 22.5	32.1	24.6	14.2	6.6	—	32.5	22.0

coast, ending up in an area of weak winds over Østlandet in the lee of Hardangervidda.

East of Trøndelag into Sweden a downstream wind shadow extends in a band with weak winds in a direction downstream from the highest mountains (Jotunheimen), approximately 20° to the right of the large-scale flow direction. The wind shadow is noticed in the three horizontal levels shown in Fig. 3, most clearly at the middle level. The scale across the structure is here 150 km when measured across the band between isotachs of 10 m s^{-1}. A minimum of 1 m s^{-1} is found approximately 750 m above ground, at steep isentropes in downstream inertio-gravity waves (Fig. 3, Section II). The direction of the local winds is rather uniform along the band structure, and no sign of vortices or return currents is found. On both sides of the shadow, the horizontal wind shear is strong, particularly on the cyclonic (right) side.

It is seen from the cross-sections (Sections II and III, Fig. 3) that the wind shadow is rather deep, generally deeper than the jet and the upstream minimum. The wind shadow is shown as a core of weak winds sloping downstream, with a wind minimum well above the local boundary layer (at 1250 m in the minimum of Section II). Winds less than 5 m s^{-1} reach to more than 1500 m. The inertio-gravity wave on the lee side of the highest mountains gives strong winds on the lee side in a shallow layer at the surface, below a deep layer of weak winds. The strong wind at the surface weakens downstream of the highest mountains.

On the right side of the wind shadow there is a secondary area with strong wind: the right-side jet. The right-side jet has a broad and shallow structure (Fig. 3, Section III). The maximum wind speed is 17 m s^{-1}, close to the middle level in Fig. 3. The upper level in Fig. 3 clearly lies above the increased wind. Rather large wind variation locally, caused by topography on the smallest scale and surface friction, masks the jet structure close to the surface.

At the surface the strong winds of the left-side jet do not reach the coast north of Romsdalsfjord. Instead we here find the coastal wind shadow as a shallow and narrow band of weak winds from Romsdalsfjord to Trondheimsfjord and over the inner area of Trondheimsfjord. The shallow shadow is only seen at the lowest level in Fig. 3 (see also cross-section AA′ in Fig. 11). The horizontal and particularly the vertical extent of the coastal wind shadow distinguishes it from the main wind shadow behind the mountain. The anticyclonic wind shear is strong towards the left-side jet. Above the shadow (upper two levels in Fig. 3), the winds are generally strong with local variations caused by gravity waves over the local mountains.

3.1.2. Large-scale winds direction beyond 230°. When the large-scale wind direction is turned towards the west, the mesoscale structures are turned with the same angle. The area of maximum wind speed of the left-side jet moves down the streamlines as the turning takes place. A turning of 10° brings the strong surface winds to the coast, all the way from Stadt to Nordland. For additional turning the jet starts to cross Nordland, causing gravity waves and strong lee winds. The amplitudes of the mesoscale structures (Table 1) show only small changes, except for the downstream wind shadow which becomes less distinct. The extension of the upstream minimum eastwards east of Lindesnes disappears because the winds get a large component from the land that reduces the effect of coastal divergence. This is the opposite effect of the coastal convergence taking place when land is to the left. The wind minimum over Østlandet is still

present. As the winds become more westerly, strong lee winds also appear east of Hardangervidda.

3.1.3. Large-scale wind direction 170°. While the flow for direction 230° everywhere—except maybe at some places at the surface—has a significant component from west, the flow for 170° gets a significant component from east. The left-side jet now accelerates northwestwards down the lee slopes of the southern parts of the mountains, with an axis that makes an angle with the coast of Vestlandet south of Stadt (Fig. 4b). The counter-clockwise turning of the jet axis (from the position at large-scale direction 230°) is approximately as the turning of the large-scale wind (60°). Maximum wind speed in the jet is now a little higher above ground; however, maximum speed at the surface is weaker (Table 1). We noticed that the jet at the surface, extending from Lista/Lindesnes (Fig. 4b), is found well southwest of the jet core. The upstream minimum is found over Østlandet with the minimum wind speed much as before. The downstream wind shadow is now found over the ocean northwest of Trøndelag. The turning of the axis is much like the turning of the large-scale flow. Minimum wind speed is now found higher above ground (compare Sections III in Figs. 3 and 4). In the middle level in Fig. 4 the shadow is found further downstream. There is clearly an area of increased wind speed to the right of the wind shadow (right-side jet). Over the sea west of Nordland the wind speed at the surface is as strong as in the left-side jet.

The lee winds are now stronger. This is especially seen at the surface over land (Fig. 4, surface), where the winds are even stronger than in the left-side jet. The strong winds are found in three bands: west of Hardangervidda, with maximum wind speed 24.0 m s^{-1}, on the lee side from Jotunheimen to Sylane, with maximum 22.0 m s^{-1} and west of the mountains in Nordland with maximum 18.5 m s^{-1}. South of Nordland, the strong lee winds found in the fjords do not reach the surface at the coast. Instead we here have a band with weak winds all the way from Boknafjord to Trondheimsfjord. The weakest winds are found between Romsdalsfjord and Trondheimsfjord, in the area of the main wind shadow. From Fig. 4, Section II, we here see steepened isentropes and minimum winds indicating wave breaking.

3.1.4. Large-scale wind direction 200°. When the large-scale wind direction is between the former two directions, the positions and axes of the mesoscale structures are likewise found between the former ones. The left-side jet now has its main axis along Vestlandet (Fig. 5, two lowest layers and Section I). The maximum strength is also in between those found earlier (Table 1). At the surface the jet flows along the coast with maximum strength just off the shoreline. The upstream minimum similarly shifts laterally to a position east of Lindesnes.

The axis of the downstream wind shadow is now from Jotunheimen towards Trondheimsfjord. The shape has changed. At the highest level it is rather broad, much as before. At the middle level it is much narrower with the axis along the coast of Trøndelag and Nordland (Fig. 5b). At this level the wind is strong on the right side of the wind shadow with maximum speed 22.0 m s^{-1}. At the surface the wind shadow is most clearly seen at the coast north of Stadt to Trondheimsfjord, and not so clearly along the axis of the shadow aloft. The weak surface wind could also be a sign of the coastal wind shadow. However, for this direction the main wind shadow and the coastal shadow tend to merge. North of Trondheimsfjord, underneath the wind shadow aloft, the wind is rather strong, with an off-shore component. However, the wind speed is weaker than for 170°. In the Møre area, the steepened isentropes (Fig. 5, Section II), indicating wave breaking, have smaller amplitudes than for wind direction 170°.

3.2. Variation with wind speed

Here we compare results from the three experiments with wind speeds of 10, 15 and 22.5 m s^{-1} for the direction 230°. Since weaker large-scale winds normally have less interest for practical weather forecasting of the wind condition, the three wind speeds cover a realistic range of flow conditions. If we let the horizontal scale be 150 km, and a mountain height $h = 1500$ m, $U = (10, 15, 22.5)$ m $^{-1}$ gives $Ro = (0.5, 0.8, 1.2)$ and $\hat{h} = (1.8, 1.2, 0.8)$. Figures 6 and 7 show similar features as Figs. 3, 4 and 5, for 10 and 22.5 m s^{-1} respectively (note that Figs. 6 and 7 only show the two lowest layers and Sections II and III). However, the winds are now given in speed-up as measured relative to the large-scale upstream wind speed above the boundary layer.

We find similar structures as discussed earlier for all the three wind speeds, particularly the left-side jet and the upstream minimum. An exception is that for stronger winds, the downstream wind shadow and the right-side jet seem to vanish at the surface (Fig. 7). The maximum and minimum wind speeds are given in Table 1. Relative to the upstream winds, the amplitudes of the wind speeds naturally decrease for increasing large-scale wind speed (h decreases and Ro increases). In the left-side jet the speed-up of the maximum wind speed relative to the strength of the upstream wind speed is 2.2 and 1.4 respectively for 10 and 22.5 m s^{-1}, compared with 1.8 for 15 m s^{-1}. This means that the change is larger per unit wind speed from 10.0 to 15.0 m s^{-1} than from 15.0 to 22.5 m s^{-1}.

3.2.1. Wind speed 10 m s^{-1}. For the lowest wind speed, the flow meets a higher effective mountain and pressure perturbations become stronger, causing stronger disturbances to the flow (Fig. 6). The Coriolis force is given a longer time to work. Relatively, the jet becomes stronger. The acceleration starts further south on the coast of Vestlandet, the axis of the jet is found further off the coast, and maximum wind speed is reached further upstream on the jet axis. The upstream minimum is similarly turned further east towards Oslofjord.

Southeasterly winds over land at Vestlandet are more pronounced, causing relatively stronger lee winds down to the Hardangerfjord and Boknafjord. Although the low-level streamlines pass over the main mountains; they are shifted more

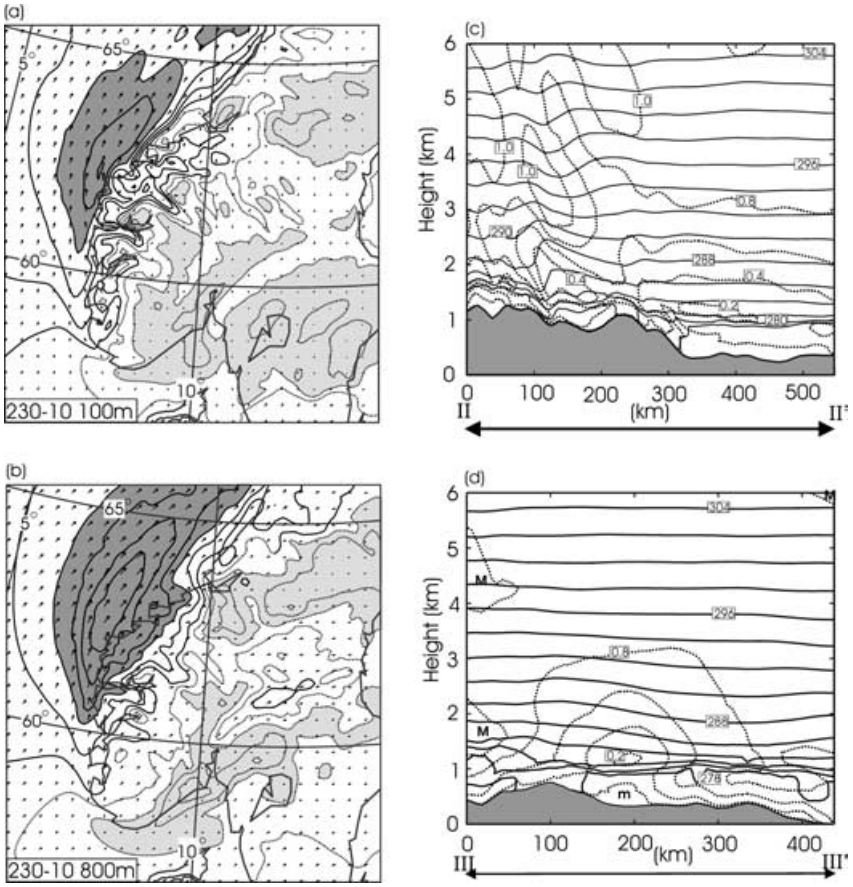

Fig 6. Horizontal wind maps for two levels (left panels) and cross-sections II and III (right panels) of potential temperature (contours every 2 K) and wind speed for large-scale wind direction 230° and speed 10 m s^{-1}. Wind speeds are given as contours of speed-up (relative to the background wind speed; contours 0.2). Upper left: surface (approximately 100 m above surface). Speed-up: solid contours, speed-up 1.0 and higher; stippled contours, 0.8 and lower. Maximum areas larger than 1.4 and minimum areas less than 0.4 are shaded grey. Sea level pressure (isobars every 2.5 hPa) gradients toward the southeast. Lower left: speed-up as above, but minimum areas less than 0.6 are shaded grey. Wind vectors are shown. Cross-sections: Upper panel, Section II; lower panel, Section III. For positions of the cross-sections, see Fig. 2b.

laterally, i.e. more air flows around the mountain. The coastal wind shadow and the downstream wind shadow are much as before in shape and position, but the downstream wind shadow starts closer to the highest mountains. The right-side jet is more pronounced.

The minimum wind speeds are low at the upstream minimum and in the downstream wind shadow (1.4 m s^{-1} at 700 m for the upstream minimum and 0.9 m s^{-1} in the shadow; see Table 1). In both places the flow is smooth with a component along the main flow direction.

3.2.2. Wind speed 22.5 m s^{-1}. A stronger wind naturally gives opposite effects (Fig. 7). The air climbs the mountain more easily, the jet starts to accelerate further north at the coast of Vestlandet, and maximum wind speed is reached further down the jet axis. The position of the upstream minimum turns westwards along the coast as a sign of decreased influence of the Coriolis force. The unity contour of the speed-up tends to extend southwards over the main mountains, in particular at the two highest levels. There are still signs of a coastal wind shadow (Fig. 7, surface). The downstream wind shadow is also still noticed at higher levels (see cross-sections in Fig. 7), but is found further downstream. There is still a weak sign of a right-side jet aloft.

4. Comparison with observational findings

The simulated wind conditions at the surface (Figs. 3, 4, 5, 6 and 7, surface) are compared with observational findings by Spinnangr (1942) and Andersen (1975). We have also prepared Fig. 8, which shows the most frequent local wind direction and typical speed at the surface at six coastal stations for large-scale wind directions at 850 hPa between south and west. Large-scale winds below 10 m s^{-1} are discarded. The wind reduction quotient in Fig. 8 is defined as local wind speed at 10 m divided by the large-scale wind speed at 850 hPa. The statistics represent 15 yr with data every 6 h. The large-scale winds are taken from reanalysis data from NCEP/NCAR (Kalnay et al., 1996) for the years 1981–1995. The reanalyses have low resolution (2.5° latitude/longitude) and show just a small effect of the Norwegian mountains. We believe the wind at 850 hPa gives an indication of actual upstream large-scale wind conditions.

4.1. The left-side jet and the upstream minimum

The main structure of the jet and the upstream wind minimum are found to be in accordance with the observational study by Andersen. He presented maps of the mean winds at synoptic

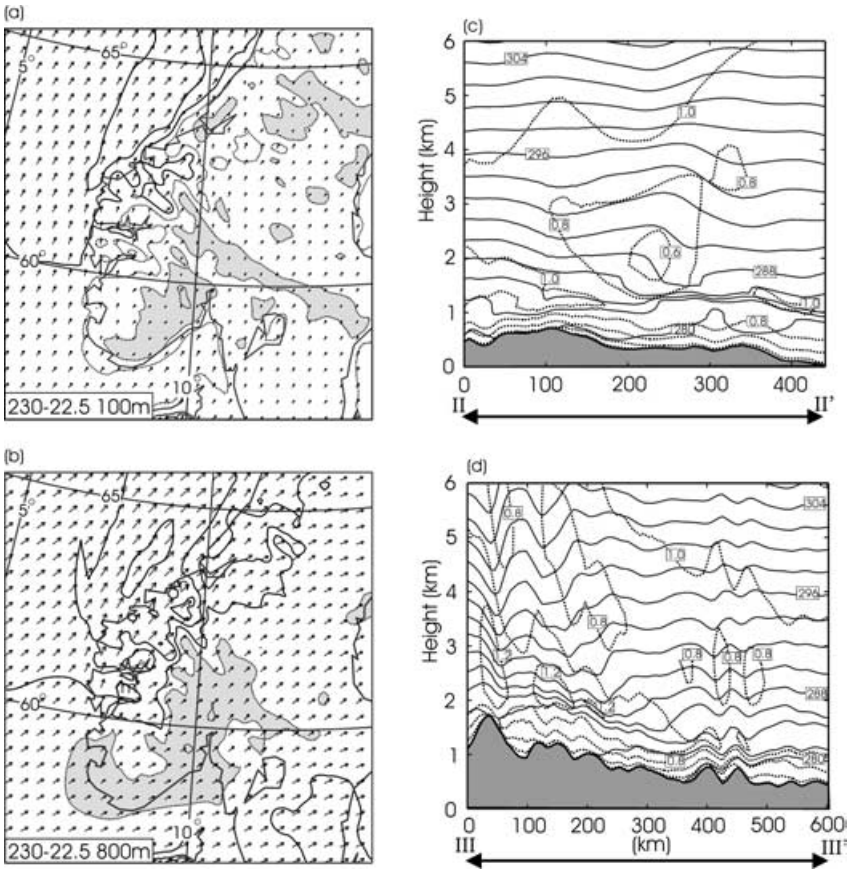

Fig 7. Same as Fig. 4, but for large-scale wind speed 22.5 m s^{-1}.

stations in southern Norway in particular months when winds from certain directions were prevailing. The maps represent large-scale directions from southeast to southwest. Based on daily observations for the period 1900–1960, he found January 1930 to be the month with maximum frequency of southwesterly geostrophic winds. The pattern of the isolines for wind speed is similar to that found for direction 200° in Fig. 5 (surface): maximum wind speed at Stadt, strong winds along the coast south of Stadt and a wind minimum over land east of Lindesnes. The map thus verifies the existence of the jet and the minimum. The mean local wind speed at Stadt was 6.5 Beaufort (∼15 m s^{-1}) and less than 1.0 Beaufort (less than 2 m s^{-1}) over land east of Lindesnes. A similar map in a month with a slightly larger westerly component (March, 1938) verifies a similar turning of the jet and the minimum. A map from November 1959 verifies the jet from the southern corner (Lindesnes/Lista) for more southerly large-scale directions. The map shows the strongest winds at the coast at Lista (see Fig. 1) and weaker winds further north. This is much as found at the surface for direction 170° in Fig. 4.

Spinnangr (1942) made his forecasting rules by investigating the local surface winds for different steady large-scale wind directions based on pressure measurements. Although he does not mention the jet directly, his findings and forecasting rules verify the jet along Vestlandet for southwesterly large-scale winds; its turning towards the coast north of Stadt as the winds turns westerly and its turning towards the coast around Lista as the direction turns towards south. He did not mention the upstream wind minimum directly, but described gradients in the wind speeds along the coast towards the minimum.

Spinnangr's description of strong southerly winds along the coast of Vestlandet is very similar to our results (Fig. 5). He was aware of the stronger winds just outside the coast and stated that the winds are one Beaufort stronger just outside the coast than at the coastal stations.

The wind reductions shown in Fig. 8 also correspond to the results above. The coastal stations Hellisøy, Ona and Sklinna are exposed to the jet, Hellisøy for directions between south and southwest, and the two others for directions between southwest and west. The strongest winds for all stations are found at Ona (sector 253–270°). The mean wind speed is as strong as the wind speed at 850 hPa (the wind quotient is 1.0). The quotient at Sklinna at the same direction is 0.77. The maximum quotient at Hellisøy is 0.88 (sector 217–234°). Also the simulations show the strongest surface winds at Ona and decreasing wind speed towards Sklinna. Compared with Hellisøy, Ona is situated further towards the open sea. When the jet is along the coast of Møre, Ona is thus relatively close to the jet axis.

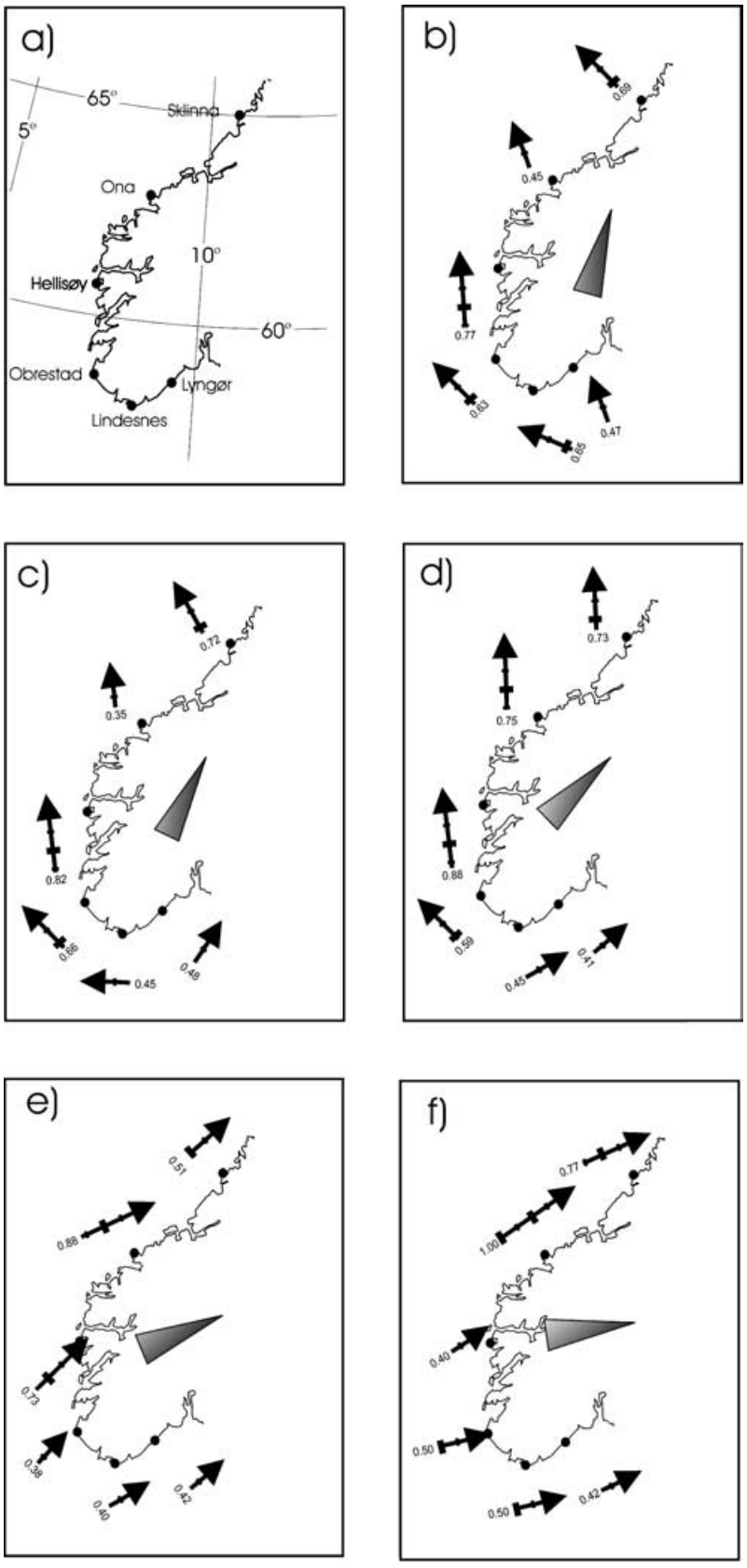

Fig 8. Local median wind direction and wind speed (tacks for every 0.25) in relation to the large-scale wind direction and speed at 850 hPa (wind speed quotient) for the following surface stations: Sklinna, Ona, Hellisøy, Obrestad, Lindesnes and Lyngør shown in (a). Fifteen years of reanalysis data from NCEP between 1981 and 1995 have been used. Cases with wind speed weaker than 10 m s^{-1} at 850 hPa are omitted. The large-scale sectors of the wind direction (at 850 hPa) are shown as a dark sector. Five sectors are chosen: (b) 181–198°, (c) 199–216°, (d) 217–244°, (e) 245–262° and (f) 263–270°.

The wind reductions at Lyngør, Lindesnes, Obrestad and Hellisøy seem to verify the upstream minimum and that it moves along the coast of Sørlandet to the southern parts of Vestlandet as the large-scale directions moves from south to west. The minimum quotients are around 0.4 in the observations.

4.2. *Coastal wind shadow at Møre*

Our findings on the wind shadow at the coast, the gradients in the wind speed between the shadow and the left-side jet and the winds north of Trondheimsfjord are qualitatively well in accordance with the forecasting rules of Spinnangr. As in our simulations (first of all Fig. 3 for direction 230°) he found the coastal wind shadow between Romsdalsfjord and Trondheimsford and relatively strong southeasterly winds on the coast north of Trondheimsfjord for southerly and south-southwesterly flows. He wrote about the turning of the jet towards the coast north of Stadt as the flows turns towards the west. He described cases similar to the one simulated from the direction 230° (Fig. 3), when the jet made a small angle with the coast. As in our results, he found that just a small turn towards west brings the winds to the coast. In particular, he described a case with southwesterly winds when ship measurements (a small fleet of fishing ships) off the coast just north of Stadt verified the strong wind gradients from the jet towards land. He reports some cases when the winds do not reach the coastal islands northeast of Stadt, south of Romsdalsfjord, but people can hear the sound of strong winds at sea. Local people call the phenomenon "Skåtung".

The wind shadow at the coast north of Stadt seems also to be qualitatively verified by Fig. 8, where the very lowest speed reduction (quotient 0.35) on all the stations is found at Ona for directions 199–216°. The stronger winds north of Trondheimsfjorden are also indicated by the quotient at Sklinna.

4.3. *Wind conditions over land on the lee side*

We have pointed out that southerly directions give strong lee winds west of Hardangervidda. This is in accordance with a forecast rule by Spinnangr, saying that the winds in the mountains in such cases are as strong as the strongest winds at the coast. We have noted that for these directions, particularly for direction 170° (see Fig. 4), there are strong winds everywhere in the mountains on the lee side, and a pronounced wind minimum at the coast, all the way from Boknafjord to Trondheimsfjord. According to Spinnangr the strong winds might penetrate down to the inner valleys and fjords. A well-known example is the strong wind on the south side of Hardangerfjord.

The work of Spinnangr is concentrated on winds on the western side of the mountains from Lindesnes to Nordland, in particular at the coast. The maps presented by Andersen give in addition some indications of the winds on the eastern side.

Wind shadows from the highest mountains into Sweden and increased wind on the right side have to our knowledge not been mentioned previously in any writings. The maps from Andersen show weak winds nearly everywhere over land and only weak indications of a main wind shadow. However, the maps clearly indicate increased surface winds over land north of Trondheimsfjord for southerly directions, much as in the model simulations (Fig. 4, direction 170°). For more westerly directions the maps from Andersen give no clear indications on the lee side of the mountains, except for increased lee wind east of Hardangervidda.

5. Discussion

An experiment without release of latent heat was made for the large-scale direction 230° and wind speed 15 m s^{-1}. It showed only small effects of latent heat release on the flow for the chosen, relatively dry humidity profile used in our experiments. Accordingly, the problem of the impact of latent heat release is not included in the discussion.

5.1. *Asymmetry—left-side jet and upstream minimum*

In agreement with theory on flows for $Ro \sim 1$(Smith 1982; Pierrehumbert and Wyman, 1985; Thorsteinsson, 1988; Thorsteinsson and Sigurdsson, 1996; Ólafsson, 2000; Petersen et al., 2003), we have demonstrated that the influence of rotation gives an asymmetric flow over southern Norway with strong winds on the left side of the mountains and a wind minimum on the right upstream side (Table 1). Naturally, the asymmetry was found to decrease with increasing upstream wind (increasing *Ro*; see horizontal maps in Figs. 6 and 7), but even for strong winds, the asymmetric behaviour was found to be a main feature of the flows.

In accordance with theory (Smith, 1982; Pierrehumbert and Wyman, 1985), we find two scales of the pressure perturbations (Fig. 9), higher pressure in front of the mountains as the air is lifted and higher pressure (but smaller amplitudes) over the main mountains. The latter perturbations have a larger scale and are also noted over the ocean. The asymmetry is explained from the pressure perturbations. The positive pressure anomalies decelerate the impinging flow, resulting in a weakened Coriolis force. The large-scale pressure gradient remains, thus air parcels are accelerated towards the left side of the mountains. As the jets detach from the corners, an adjustment towards geostrophic balance takes place. In this process the jet is turned towards the direction of the isobars (compare flows in Figs. 3, 4 and 5 with pressure fields in Fig. 9).

Increased winds on the left side were found over a broad area. For southwesterly winds (200°, Fig. 5), the axis of the jet was found along the coast of Vestlandet south of Stadt. For more westerly (southerly) winds, the main part of the jet was found over the sea, downstream of the corner at Stadt (Lindesnes/Lista) (Figs. 3 and 4). The maximum wind speed of the left-side jet and the upstream minimum did not change much as the wind direction was changed for a constant large-scale wind speed of 15 m s^{-1} (Table 1). This is surprising since the influence of

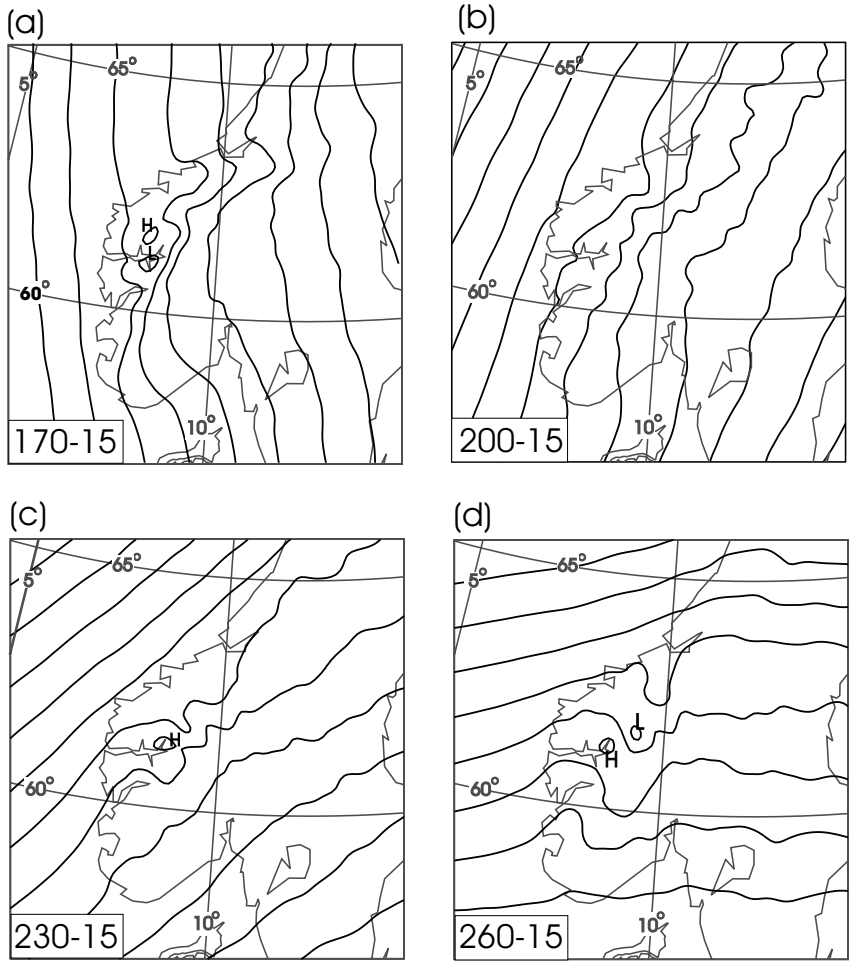

Fig 9. Sea level pressure (contours every 2.5 hPa) for four large-scale wind directions and wind speed 15 m s^{-1}.

the Coriolis force on the perturbations will vary as the flow direction changes, i.e. the flow feels a different mountain as the wind turns.

Consider the influence of rotation in flows with $Ro \sim 1$ over an idealized obstacle with contours shaped as ellipses (see Fig. 10). Let the extended axis be towards the north. Assume flows either from southwest or southeast with the same strength. Further, assume that the pressure perturbations set up are symmetric around the south–north axis, as they are in a linear flow (we have verified that by running a linear model for such flows). The incoming particles are decelerated similarly in both cases, but the subsequent ageostropic acceleration towards the left feels different mountains. A particle approaching the high pressure from the southwest, will—as the Coriolis force is decreased—first be accelerated away from the mountain by the background pressure gradient. Then, as the Coriolis force again becomes stronger, the particle will turn northwards along the slope. Eventually, the air will climb the mountain. The action of the Coriolis force in this way strengthens the flow over the mountain (the flow will face a narrower mountain). On the other hand, a particle approaching the high pressure from southeast will first be accelerated towards the mountain, and the lifting will hamper the acceleration. When the particle enters the lee side, it will run downhill gaining kinetic energy. Altogether, the action of the Coriolis force weakens the flow over the mountain and gives a wind maximum on the lee side (wider mountain). Southeasterly flows will thus be more easily blocked than southwesterly flows.

The mountains of southern Norway are of course more complex. All flows with directions from 200 to 270° will, however, show similarities with the southwesterly flow described above. The explanation lies in the regular curvature of the large-scale terrain contours around the corner at Stadt. As the flow direction is changed towards the west, the angle between the background flow and the main contours remains similar. In addition, the scale along the contours will be larger than the scale across the mountain perpendicular to the contours. In this way the mountain felt by the flows does not change radically when the flow comes from the southwest sector. The similarities might explain the small variations in the maximum wind speed in the left-side jet for directions from 200 to 270° (Table 1).

When the flow gets a component from the east in lower layers (Fig. 4), the flow experiences a wider mountain, much as in the southeasterly flow described above. The wide mountain gives significantly stronger lee winds than for southwesterly flows. Steeper slopes on the western than the eastern side will contribute in the same direction. Opposite to southwesterly flows, the left-side jet—as shown in the middle level of Fig. 4b—gets most of its acceleration down the lee slopes. In fact, it becomes stronger than for the other directions (see Table 1). However, the jet does not penetrate to the surface because wave activity brings a band of minimum wind speed along the coast from Boknafjord and northward to Trondheimsfjord (isentropes analogous to hydraulic jumps). At the surface the strongest winds are found further southwest, from Lindesnes/Lista, where the wave activity is less dominant. The maximum wind speed is a bit weaker than for southwesterly large-scale flow directions (Table 1).

Stronger winds were naturally found at the surface just off the coast due to smaller surface friction over the ocean. When land was to the right of the flow, we found coastal convergence due to differential roughness at the coastline (e.g. Alestalo and Savijärvi, 1985). In addition, the differential cooling at the surface formed a shallow front (Fig. 4, Section I) along the coast causing cross-shore circulation and additional convergence. It is difficult to quantify the amount of the convergence that comes from the difference in surface friction and that originating from the differential heating. The resulting convergence strengthened the jets over the sea and caused bands of precipitation along the coast as indicated by Bergeron (Godske et al. 1957). A simulation with mountains but no roughness change across the coast shows that the roughness change and differential heating contribute to the jet structure and the steering of the jet along the coast (not shown). From tests performed with idealized shallow and steep coasts (not shown), the steepness of the slopes gives a similar steering effect. This view is supported by Overland and Bond (1993).

Spinnangr explained the wind maximum off the coast as an effect of coastal convergence in southerly winds. This explanation was also given by Bergeron (Godske et al. 1957). We also consider coastal convergence to play a significant role; however, the strong winds are first of all a result of the jet on the left side of the mountains.

5.2. *Flow regimes*

In non-rotational flows, onset of upstream stagnation and flow splitting are clear signals of a regime change (Smith 1989a). Also in rotational flows, sufficiently high mountains cause upstream blocking and flow splitting, Thorsteinsson and Sigurdsson (1996). Our simulations with an upstream wind speed of 15 m s^{-1}, showed definitely no upstream stagnation above the lowest model layer. For a large-scale wind direction of 230° and speed 10 m s^{-1}, the flow was close to stagnation upstream, but complete blocking and flow splitting did not take place (Table 1). In flows without rotation, flow splitting would in this case be expected, since $\hat{h} = 1.8$, i.e. higher than the threshold for blocking to take place (Smith and Grønås, 1993). Thus our simulations for southwesterly winds suggest that the influence of rotation is delaying the onset of upstream blocking as the efficient mountain height is increased. This is in accordance with our discussion above in Section 5.1 and Thorsteinsson and Sigurdsson (1996).

In our findings, the main wind deficits behind the mountain have been referred to as the wind shadow. The axis of the structure was found to be far longer along the flow than across. Flows free of rotation may have wakes. Smolarkiewicz and Rotunno (1989) defined a wake as a region of decelerated air mass downstream of an obstacle, possibly with reversed flow. Following their definition, a wake may be produced by baroclinic tilting terms in a fluid without surface friction. Smith (1989b) disputed their view and proposed a definition in which wakes can originate from dissipation only. According to Smith's definition, an upstream stagnation point may lead to dissipation and formation of a wake. Our simulations showed wakes according to the definition of Smolarkiewicz and Rotunno (1989), but no blocking took place. For southwesterly directions, substantial wave breaking was not found either. Trüb and Davies (1995) reported strong a orogenic response behind a ridge in presence of inertio-gravity waves. For $Ro = 3$ and $\hat{h} = 1$, they found the strength

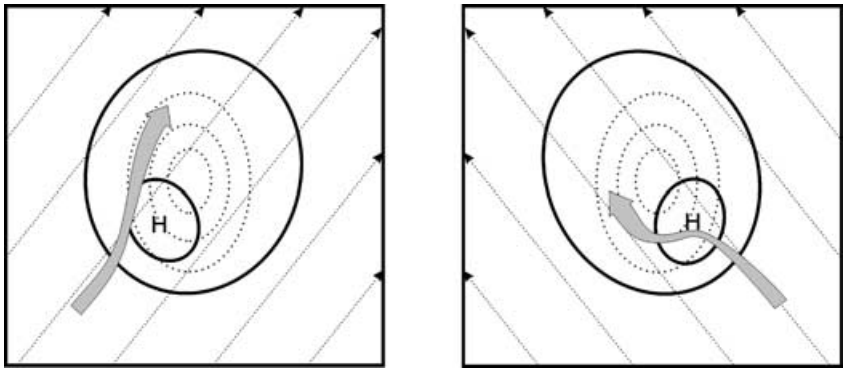

Fig 10. Conceptual illustration of the flows around an elongated mountain (dashed contours) in the intermediate domain ($Ro \sim 1$ and $\hat{h} \sim 1$). Perturbation isobars are indicated as solid lines, and the width of the arrows indicates the wind speed. The upstream flow (dotted straight lines) comes from (left) southwest and (right) southeast.

of wind perturbations, in a direction opposite to the background flow, to be of similar a magnitude as the background flow. As discussed below, we find inertio-gravity waves to play a major role in forming the wind shadow. We do not believe that dissipation is the main component in the formation of the wind shadow.

5.3. *The downstream wind shadow*

For all wind speeds and directions investigated, the flows passed over the central mountains, and the flow regime was characterized by gravity and inertio-gravity waves. Near parabolic zones trailed from each side of the mountains out over the sea and flat areas over Sweden (see upper level in Figs. 3, 4, 5). The structures are similar to those described by Smith (1980).

Downstream of the highest mountains, inertio-gravity waves inflicted a deep slanting layer of weak winds above the boundary layer that formed the wind shadow (Sections II and III, Figs. 3, 4 and 5). This rather deep layer was found some distance from the central mountain tops. The layer—except for the strongest wind speed—was also experienced down to the surface. However, wave activity connected to smaller-scale mountains distorted the signal. For sufficiently weak upstream southerwesterly winds and for southerly directions, the isentropes in the layer became very steep and the horizontal wind speed close to zero. Such signs of breaking waves were connected to strong lee winds at the steepest slopes and found towards the bottom of the slopes.

The wind shadow became less distinct when the winds turned towards the west. The reason is a shorter scale across the mountain (higher *Ro*) for westerly than for southwesterly winds. Accordingly, there is less influence of rotation on the gravity waves. With stronger winds the inertio-gravity waves naturally became less distinct, and the area of weaker winds was lifted from the ground.

We found an area of increased winds at the right side of the wind shadow; the right-side jet (Section III, Figs. 3, 4 and 5). We think that the jet is formed in the adjustment to restore geostrophic balance downstream of the main mountains. Further explanation remains for future studies.

In accordance with theory, we found signs of hydrostatic gravity waves without influence of rotation over the smallest mountain scales. Such waves have their group velocity pointing vertically (Section II in Figs. 3–7). Longer waves, influenced by rotation (inertio-gravity waves) and with group velocities pointing more downstream, were found on the lee side of the larger-scale mountains. The limiting frequency of the induced disturbance is the Coriolis parameter, i.e. $f \sim Uk \sim U/L$, where L is the length scale and k is the horizontal wave number. Beyond this cut-off limit, which correspond to $Ro = 1$, the divergence of the momentum field is overwhelmed by the deflection of the Coriolis force. For $L = 150$ km and $f = 10^{-4}$ s^{-1}, the cut-off happens for $U = 15$ m s^{-1}, when the vertical wave number becomes singular with an infinite wave number. In other words, for this wind speed wavelengths longer than $L = 150$ km do not contribute to gravity wave activity. As the wind speed decreases, shorter waves will force the gravity wave activity. Below we discuss the question of which wavelengths dominate the formation of the downstream wind shadow. The phase lines connected to the inertio-gravity waves, that formed the wind shadow, tilt downstream. Applying 2-D linear theory from Gill (1982) and Trüb and Davies (1995), it can be shown that the phase line for the first downstream minimum, slanting toward the ground, is given by:

$$z = -(f/N)(Ro^2 - 1)^{1/2}\left(x - \frac{3\pi L}{2}\right), \tag{1}$$

where the x-axis is oriented from the ridge centre. For a given U, stronger stability or smaller L makes the phase line steeper. For southwesterly large-scale directions, e.g. directions 200 and 230°, and wind speed 15 m s^{-1}, a forcing from a terrain with L around 50 km seems to fit the simulated slanting angle for the downstream wind shadow. The corresponding mountain should be the mountain area of Jotunheimen.

We have seen that as the wind direction was turned, the response of the inertio-gravity wave changed significantly. This suggests that forcing of the wind shadow comes from several wavelengths, maybe in a non-linear interaction. Furthermore, the use of background values of N and U in eq. (1) is somewhat ambiguous. These values are likely to be modified by the flow, so the linear response in eq. (1) must be looked upon with great care.

We noticed that the axis of the downstream wind shadow did not extent directly along the direction of the undisturbed flow, but formed an angle to the right. An adjustment towards geostrophic balance takes place in the area. In the wind shadow the geostrophic wind is directed along the shadow. Accordingly, there is a low-pressure perturbation on the right side of the flow (Fig. 9). Petersen et al. (2003) indicated that the circulation of such low-pressure perturbations contributes to their advection towards a more southerly position, and this might explain the turning of the wind shadow axis towards the right.

5.4. *The coastal wind shadow*

In addition to the downstream wind shadow, a shallow area of weak winds was found at the coast of Møre for southwesterly directions. We called this the coastal wind shadow, and it was found to be a kind of elongated wake, where the wind direction was along the longest axis. For the direction 200°, the main wind shadow and the coastal wind shadow tended to merge. When the flow got a more westerly component (Fig. 3), the two structures separated, with clearly different depths.

We believe that the coastal shadow is caused by differential friction, land/sea and dissipation, either by breaking waves downstream of the steep slopes at Møre or surface friction. To the

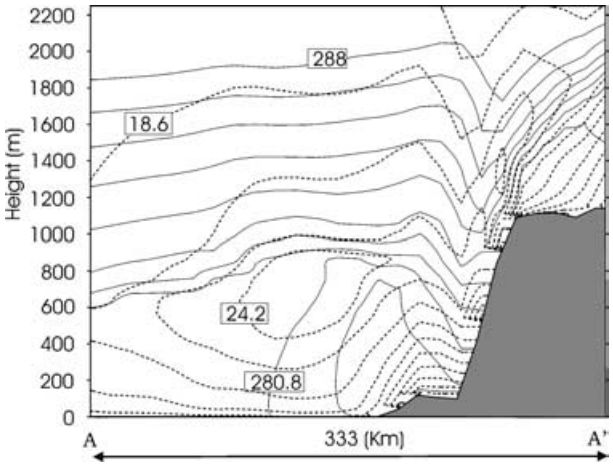

Fig 11. Cross-section (A–A′) of potential temperature (contours every 2 K) and wind speed (contours every 2.5 m s^{-1}) through the coastal wind shadow at Møre. Large-scale wind is 230° and 15 m s^{-1}. The position of the section is shown in Fig. 2 lower panel.

extent that breaking waves occur downstream of the large-scale mountains, generation of PV banners inevitable and an accompanying drop in the Bernoulli function results (Schär, 1993; Schär and Smith, 1993). Hence, air flowing over the mountain, experiencing a drop in Bernoulli function, has a lower total energy than the air passing in the jet, air that has not passed any mountain.

Figure 11 shows a cross-section through the shallow shadow at Møre for the large-scale direction 230°. The shallow structure is typically less than 1 km deep. Above the weak winds close to surface, gravity waves have large amplitudes. Breaking waves, both here and further upstream, might explain a wind reduction along a trajectory through the breaking area. Aircraft pilots are well acquainted with turbulence in similar flow situations under take-off and landing at Vigra airport, just north of Stadt.

For southerly directions an area of weak winds was found along the coast all the way from Boknafjord to Trondheimsfjord (Fig. 4a). This structure did not have the same character as the coastal wind shadow, since the wind direction was from land across the minimum belt. In this case the wind minimum was caused by wave activity, where breaking waves might have been present.

6. Summary and concluding remarks

We have studied results from numerical experiments of ideally constructed southwesterly flows over southern Norway, conditions frequently producing gales somewhere along the coast. The results are found to be in qualitative agreement with studies based on surface observations at the coast and over land. In particular, the asymmetric flow caused by rotation, with strong winds on the left side of the flow and a wind minimum at the upstream right-hand side of the flow, is found to agree with surface observations at the coast and old forecasting rules.

A deep, wind shadow was found downstream of the highest mountains with signs of an area of increased winds on the right side. The shadow is not a classical wake found downstream of smaller, high mountains, but a result of rotational effects on the gravity waves. A secondary, much shallower, wind shadow was also found at the coast, in particular between Romsdalsfjord and Trondheimsfjord for southwesterly wind directions. It is probably caused by differential friction, land/sea and dissipative mechanisms behind steep mountains.

When the large-scale wind direction was turned, the axes of the jet and the downstream wind shadow and the position of the upstream minimum turned similarly. For the large-scale direction of 200°, the left-side jet was along the coast of Vestlandet south of Stadt. For a turning in the wind direction towards west, the jet was connected to the corner around Stadt. Beyond 230°, the jet reached the coastline of Møre. For the mentioned directions, the acceleration of the jet took place along or parallel to the large-scale mountain contours. Further, the action of the Coriolis force on the perturbations helped the flow over the mountains. In this way, for southwesterly flows, they became effectively narrower than without rotation. Southerly winds gave a significant component from the east in the boundary layer. The action of the Coriolis force then gave a component towards the mountains, and the acceleration of the left-side jet took place down the lee slopes. Altogether, the influence of the Coriolis force made the mountains effectively wider than without rotation. The maximum wind speed at the surface in jets connected to Stadt was found to be slightly stronger than in those connected to Lindesnes/Lista.

The gravity waves and the lee winds were stronger for southerly than for southwesterly winds. The reason for this is related to the relatively wide mountains for southerly directions and the steeper lee slopes. The strong lee winds were found all the way from Boknafjord to Trondheimsfjord. At the surface, the maximum lee wind speeds were stronger than in the left-side jet. The wind over the sea on the right side of the wind shadow (north of Trøndelag and west of Nordland) was as strong as in the left-side jet.

There are virtually no observations to verify the simulated flows aloft and over the sea. The significance of new information about wind over the sea inverted from satellite measurements (scatterometer and SAR winds) should be investigated. Observations indicating the vertical structure of the jet should be made available (radar, wind profilers and flight measurements etc.). The downstream main shadow has not been mentioned previously in the literature. Wind variation at exposed surface stations in Norway and Sweden should first be investigated in order to verify its existence. However, wind measurements aloft will be needed to check the depth of the structure.

In this paper, we have concentrated on the validation of simulated flow structures against observational findings under typical flow conditions. An atmospheric model with normal parametrization of friction and diabatic effects has been used.

Accordingly, it has been difficult to isolate different physical effects on the flow, such as rotation, friction, change in friction and different diabatic effects. Our dynamical explanation of the flow behaviour has thus not reached a satisfactory level. For one of the large-scale directions we have made cleaner experiments in order to discuss the relative importance of the mentioned effects. This will be presented in a forthcoming paper.

7. Acknowledgments

The authors thank the reviewers and Professor R.B. Smith for highly valuable discussions. We will also thank Mr I. Hessevik for IT support and The Norwegian Meteorological Institute, in particular Dr E. Berge and Dr A. Sorteberg, for support of various kinds. The Institute for Energy Technology (IFE), Kjeller, Norway has financed much of the work. Supercomputing resources have been made available by The Norwegian Research Council.

References

Alestalo, M. and Savijärvi, H. 1985. Mesoscale circulations in a hydrostatic model: coastal convergence and orographic lifting. *Tellus* **37A**, 156–162.

Andersen, P. 1973. The distribution of monthly precipitation in Southern Norway in relation to prevailing H. Johansen weather types. *Årbok Universitet Bergen, Mat. Naturv. Ser.*, 1–20.

Andersen, P. 1975. Surface winds in southern Norway in relation to prevailing H. Johansen weather types. *Meteor. Ann.* **6**(14), 377–399.

Baines, P. G. 1995. *Topographic Effects in Stratified Flows*. Cambridge University Press, New York.

Bjerknes, J. and Solberg, H. 1921. Meteorological conditions for the formation of rain. *Geofys. Publ.* **2**(3).

Bjerknes, J. and Solberg, H. 1922. Life cycle of cyclones and polar front theory of the atmospheric circulation. *Geofys. Publ.* **3**(1), 1–18.

Blackadar, A. 1979. High resolution models of the planetary boundary layer. In: *Advances in Environmental Sciences and Engineering* Vol. 1 (eds E. N. Pfaffin and J. R. Ziegler). Gordon and Breach, New York, 50–85.

Burk, S. and Thompson, H. 1989. A vertically nested regional numerical prediction model with second-order closure physics. *Mon. Weather Rev.* **117**, 2305–2324.

Dudhia, J. 1989. Numerical study of convection observed during the winter monsoon experiment using a mesoscale two-dimensional model. *J. Atmos. Sci.* **46**, 3077–3107.

Gill, A. E. 1982. *Atmosphere–Ocean Dynamics*, International Geophysics Series, Academic Press, New York.

Godske, C., Bergeron, T., Bjerknes, J. and Bundgaard, R. 1957. *Dynamic Meteorology and Weather Forecasting*. American Meteorological Society and Carnegie Institution of Washington, Washington, DC.

Grell, G., Dudhia, J. and Stauffer, D. 1994. *A Description of the Fifth-generation Penn State/NCAR Mesoscale Model (MM5).* NCAR Technical Note NCAR/TNN-398+STR. NCAR, Boulder, CO.

Hunt, J. C. R., Ólafsson, H. and Bougeault, P. 2001. Coriolis effects on orographic and mesoscale flows. *Q. J. R. Meteorol. Soc.* **127**, 601–633.

Kalnay, E., Kanamitsu, M., Kistler, R., Collins, W., Deaven, D. et al. 1996. The NCAR/NCEP 40-years reanalysis projects. *Bull. Am. Meteorol. Soc.* **77**, 437–471.

Nordø, J. and Hjortnæs, K. 1966. Statistical studies of precipitation on local, national and continental scales. *Geofys. Publ.* **26**(12).

Ólafsson, H. 2000. The impact of flow regimes on asymmetry of orographic drag at moderate and low Rossby numbers. *Tellus* **52A**, 365–379.

Ólafsson, H. and Bougault, P. 1996. Nonlinear flow past an elliptic mountain ridge. *J. Atmos. Sci.* **53**, 2465–2489.

Ólafsson, H. and Bougault, P. 1997. The effect of rotation and surface friction on orographic drag. *J. Atmos. Sci.* **54**, 193–210.

Overland, J. E. and Bond, N. 1993. The influence of coastal orography: the Yakutat storm. *Mon. Weather Rev.* **121**, 1388–1397.

Petersen, G. N., Ólafsson, H. and Kristjánsson, J. E. 2003. Flow in the lee of idealized mountains and Greenland. *J. Atmos. Sci.*, **60**, 2183–2195.

Pierrehumbert, R. and Wyman, B. 1985. Upstream effects of mesoscale mountains. *J. Atmos. Sci.* **42**, 977–1003.

Schär, C. 1993. A generalization of Bernoulli's theorem. *J. Atmos. Sci.* **50**, 1437–1443.

Schär, C. and Smith, R. B. 1993. Shallow water flow past isolated topography. Part I: Vorticity production and wake formation. *J. Atmos. Sci.* **50**, 1373–1400.

Smith, R. B. 1979. The influence of mountains on the atmosphere. *Adv. Geophys.* **21**, 87–230.

Smith, R. B. 1980. Linear theory of stratified hydrostatic flow past an isolated mountain. *Tellus* **32**, 348–364.

Smith, R. B. 1982. Synoptic observation and theory of orographically disturbed wind and pressure. *J. Atmos. Sci.* **39**, 60–70.

Smith, R. B. 1989a. Hydrostatic airflow over mountains. *Adv. Geophys.* **31**, 59–81.

Smith, R. B. 1989b. Comment on "Low Froude number flow past three-dimensional obstacles. Part I: Baroclinically generated lee vortices" by P. K. Smolarkiewicz and R. Rotunno. *J. Atmos. Sci.* **46**, 3611–3613.

Smith, R. B. and Grønås, S. 1993. Stagnation points and bifurcation in 3-D mountain flow. *Tellus* **45A**, 28–43.

Smolarkiewicz, P. K. and Rotunno, R. 1989. Low Froude number past three-dimensional obstacles. Part I: Baroclinically generated lee vortices. *J. Atmos. Sci.* **46**, 1154–1164.

Smolarkiewicz, P. K. and Rotunno, R. 1990. Low Froude number past three-dimensional obstacles. Part II: Upwind flow reversal zone. *J. Atmos. Sci.* **47**, 1498–1511.

Spinnangr, F. 1942. On the influence of the orography on the winds in southern Norway. *Bergens Museums Årbok Naturv. Rekke* number 3.

Spinnangr, F. 1943a. Synoptic studies on precipitation in southern Norway. I. Instability showers. *Meteor. Ann.* **1**, 323–356.

Spinnangr, F. 1943b. Synoptic studies on precipitation in southern Norway. II. Front precipitation. *Meteor. Ann.* **1**, 433–468.

Thorsteinsson, S. 1988. Finite amplitude stratified air flow past isolated mountains on an f-plane. *Tellus* **40A**, 220–236.

Thorsteinsson, S. and Sigurdsson, S. 1996. Orogenic blocking and deflection of stratified air flow over an f-plane. *Tellus* **48A**, 578–583.

Trüb, J. and Davies, H. 1995. Flow over mesoscale ridge: pathways to regime transition. *Tellus* **47A**, 502–524.

Zhang, D.-L. and Anthens, R. 1982. A high resolution model of the planetary boundary layer sensitivity tests and comparisons with SESAME-79 data. *J. Appl. Meteorol.* **21**, 1594–1609.